The Astrophysical Journal, 908:105 (7pp), 2021 February 10 https://doi.org/10.3847/1538-4357/abd326
© 2021. The American Astronomical Society. All rights reserved.

A Single-pulse Study of PSR J1022+1001 Using the FAST Radio Telescope

Yi Feng[1,2,3], G. Hobbs[3], D. Li[1,2,4], S. Dai[3], W. W. Zhu[1], Y. L. Yue[1], P. Wang[1], S.-B. Zhang[2,3,5], L. Qian[1], L. Zhang[1,2,3], S. Q. Wang[6], C. C. Miao[1,2], M. Yuan[1,2], and Y.-K. Zhang[1,2]
[1] CAS Key Laboratory of FAST, National Astronomical Observatories, Chinese Academy of Sciences, Beijing 100101, People's Republic of China; yifeng@nao.cas.cn
[2] University of Chinese Academy of Sciences, Beijing 100049, People's Republic of China
[3] CSIRO Astronomy and Space Science, P.O. Box 76, Epping, NSW 1710, Australia
[4] NAOC-UKZN Computational Astrophysics Centre, University of KwaZulu-Natal, Durban 4000, South Africa
[5] Purple Mountain Observatory, Chinese Academy of Sciences, Nanjing 210008, People's Republic of China
[6] Xinjiang Astronomical Observatory, 150, Science-1 Street, Urumqi, 830011 Xinjiang, People's Republic of China
Received 2020 July 26; revised 2020 December 4; accepted 2020 December 10; published 2021 February 17

Abstract

Using the Five-hundred-meter Aperture Spherical radio Telescope (FAST), we have recorded $\sim 10^5$ single pulses from PSR J1022+1001. We studied the polarization properties, their energy distribution, and their times of arrival. This is only possible with the high sensitivity available using FAST. There is no indication that PSR J1022+1001 exhibits giant pulse, nulling, or traditional mode changing phenomena. The energy in the leading and trailing components of the integrated profile is shown to be correlated. The degree of both linear and circular polarization increases with the pulse flux density for individual pulses. Our data indicates that pulse jitter leads to an excess noise in the timing residuals of 67 ns when scaled to one hour, which is consistent with Liu et al. We have unsuccessfully trialed various methods to improve timing precision through the selection of specific single pulses. Our work demonstrates that FAST can detect individual pulses from pulsars that are observed in order to detect and study gravitational waves. This capability enables detailed studies, and parameterization, of the noise processes that affect the sensitivity of a pulsar timing array.

Unified Astronomy Thesaurus concepts: Pulsars (1306); Astronomy data analysis (1858)

1. Introduction

Radio pulsars are known to exhibit a profusion of emission phenomena. For instance, mode changing (e.g., Bartel et al. 1982; Wang et al. 2007), nulling (e.g., Backer 1970; Wang et al. 2007), sub-pulse drifting (e.g., Drake & Craft 1968; Weltevrede et al. 2006), and giant pulse (e.g., Staelin & Reifenstein 1968; Hankins et al. 2003) phenomena have been observed in normal pulsars. The profile shapes of individual pulses vary significantly (e.g., Jenet et al. 2001; Shannon & Cordes 2012), but the summation of a large number of pulses usually leads to a stable profile. Mode changing is a discontinuous change where the mean pulse profile abruptly changes between two (or sometimes more) quasi-stable states. Nulling is where individual pulses in the pulse train are undetectable. Individual pulses can be tens or hundreds of times brighter than the average, which is known as giant pulse phenomenon. Giant pulses are much narrower than the average profile and have durations that range from nanoseconds to microseconds and follow a power-law energy distribution. With this definition, giant pulses have been detected in seven pulsars, including two young pulsars and five millisecond pulsars (e.g., Staelin & Reifenstein 1968; Cognard et al. 1996; Johnston & Romani 2003). Mode changing and nulling are thought to be linked and are caused by changes in the pulsar magnetosphere (Lyne et al. 2010; Stairs et al. 2019).

Mode changing, nulling, and sub-pulse drifting phenomena are relatively rare in millisecond pulsars (MSPs). Mode changing has been observed in only one MSP (Mahajan et al. 2018), nulling has not yet been reported and sub-pulse drifting has been observed in only three MSPs (Edwards & Stappers 2003; Liu et al. 2015). This cannot be fully explained by selection biases caused by a lack of well studied single pulses from MSPs (e.g., Jenet et al. 2001; Shannon & Cordes 2012; Osłowski et al. 2014; Liu et al. 2016).

In this paper, we carried out a single-pulse study of PSR J1022+1001. We have recorded over $\sim 10^5$ single pulses from PSR J1022+1001 with the Five-hundred-meter Aperture Spherical radio Telescope (FAST, Nan et al. 2011; Li & Pan 2016). PSR J1022+1001 has a pulse period of 16.45 ms and a dispersion measure (DM) of 10.2 cm^{-3} pc. The scintillation bandwidth and timescale for this pulsar are 65 MHz and 2334 s, respectively, at 1400 MHz (Keith et al. 2013). The pulsar is in a binary system with a 7.8 days orbital period with a white dwarf companion. The average pulse profile obtained from our FAST observation is shown in Figure 1. The integrated pulse profile of PSR J1022+1001 consists of two components in the 20 cm band with a highly linearly polarized trailing component.

The stability of the integrated profile for PSR J1022+1001 has been studied in detail. Kramer et al. (1999) showed that the amplitude ratio of the two components evolves on short timescales (tens of minutes). Hotan et al. (2004a) argued that profile instability could also arise from improper polarization calibration because of an imperfect receiver model. Liu et al. (2015) showed that improper polarization calibration and diffractive scintillation cannot be the sole reason for the observed profile instability. Shao & You (2017) argued that profile instability is mainly caused by the evolution of the pulse profile with frequency combined with the interstellar scintillation. Recently, with long term observations at Effelsberg Radio Telescope, Padmanabh et al. (2020) found that the pulse shape variations cannot be fully accounted for by instrumental and propagation effects and suggested additional intrinsic effects as the origin for the variation.

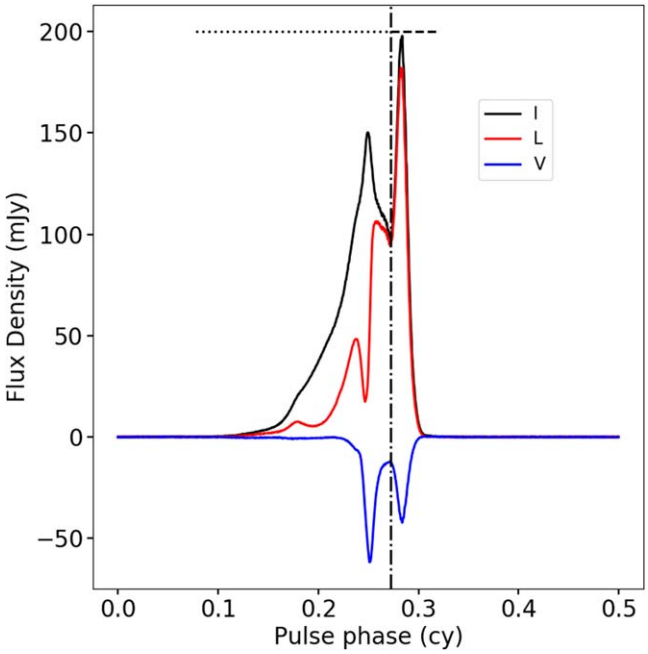

Figure 1. Averaged polarization profile of PSR J1022+1001. The black, red, and blue lines represent Stokes *I*, the linear polarization and Stokes *V*, respectively. We define the phase ranges identifying the leading and trailing components using the horizontal and vertical lines (chosen to agree with Liu et al. 2015 and to be the minimum between the two peaks in the profile). The on-pulse region is taken to be the range delimited by the leading and trailing components.

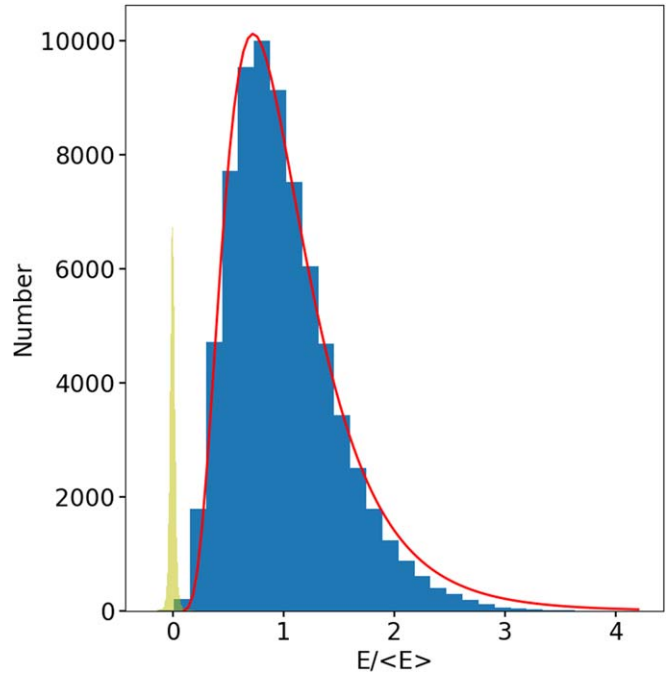

Figure 2. Pulse energy histograms for the off-pulse region (yellow) and on-pulse region (blue). The pulse energies are normalized by the mean on-pulse energy. The red line is a log-normal distribution that has been fitted to the on-pulse energy histogram.

Our observations and data processing procedures are described in Section 2. Our results are presented in Section 3. We conclude and discuss our results in Section 4.

2. Observation and Data Processing

For our analysis, we selected one of the brightest observations of PSR J1022+1001 from a FAST early science project (PID 3005). We obtained 7.3×10^4 single pulses in a 20 minutes observation on MJD 58749. The observation was conducted using the central beam of the 19-beam receiver (Jiang et al. 2019). The 19-beam receiver, with the frequency range between 1050 and 1450 MHz, provides two data streams (one for each hand of linear polarization). The data streams are processed with the Reconfigurable Open Architecture Computing Hardware version 2 (ROACH2) signal processor (Jiang et al. 2019). The output data files are recorded as 8 bit-sampled search mode PSRFITS (Hotan et al. 2004b) files with 4096 frequency channels and with 49.152 μs time resolution.

We used the DSPSR software package (van Straten & Bailes 2011) to extract individual pulses. The "-K" option of the DSPSR software package was used to remove inter-channel dispersion delays. Polarization calibration was achieved by correcting for the differential gain and phase between the receptors through separate measurements of a noise diode signal injected at an angle of 45° from the linear receptors. We determined a rotation measure (RM) of 2.9 ± 0.2 rad m^{-2} from our data and the profiles are RM-corrected. The observations were then flux density calibrated using observations of 3C 286 (Baars et al. 1977). To excise radio frequency interference, we used the PSRCHIVE software package (Hotan et al. 2004b) to median filter each single pulse in the frequency domain. Band-averaged analytical templates were made using the profile obtained when an entire observation was folded. We used the PSRCHIVE and TEMPO2 (Hobbs et al. 2006) software packages to determine pulse times of arrival (ToAs) and timing residuals for each single pulse using the timing model from Kerr et al. (2020).

Our calibration procedure produces an integrated pulse profile, shown in Figure 1, that agrees with previously published profiles (for instance, Dai et al. 2015).

3. Results

We first present our results from analyzing the single-pulse energy distributions and our search for correlations between the leading and trailing profile components. We then search for the presence of giant pulse, nulling, or traditional mode changing phenomena. We study the polarization properties of the single pulses. Finally, we measure the jitter noise and trial various methods to improve the timing precision by only selecting a sub-set of the single pulses.

3.1. Single-pulse Statistics

We define the energy of each single pulse (in non-physical units) to be its integrated flux density. For each pulse, this is determined by measuring the area across the on-pulse region (see ranges in Figure 1). We also defined an off-pulse window that was used as a control sample to assess the statistics of the noise in our measurements. The off-pulse window was chosen to have the same width as the on-pulse region. We normalized energy of each pulse by the mean value in the on-pulse region $\langle E \rangle$. The results are shown in Figure 2. The yellow histogram shows the off-pulse energy distribution and the noise in the off-pulse region follows the expected normal distribution. The blue histogram shows the on-pulse energy distribution, which is well fit (see red line in Figure 2) by a log-normal distribution of

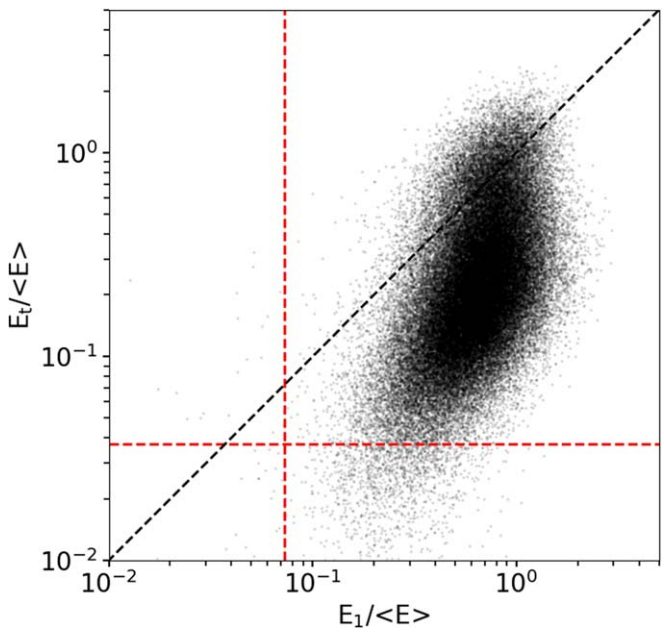

Figure 3. Correlation of the leading component pulse energy and trailing component pulse energy. The pulse energies are normalized by the mean on-pulse energy. The vertical and horizontal red dashed lines represent the 3σ noise levels of the leading and trailing component, respectively. The black dashed line represents $E_t = E_l$.

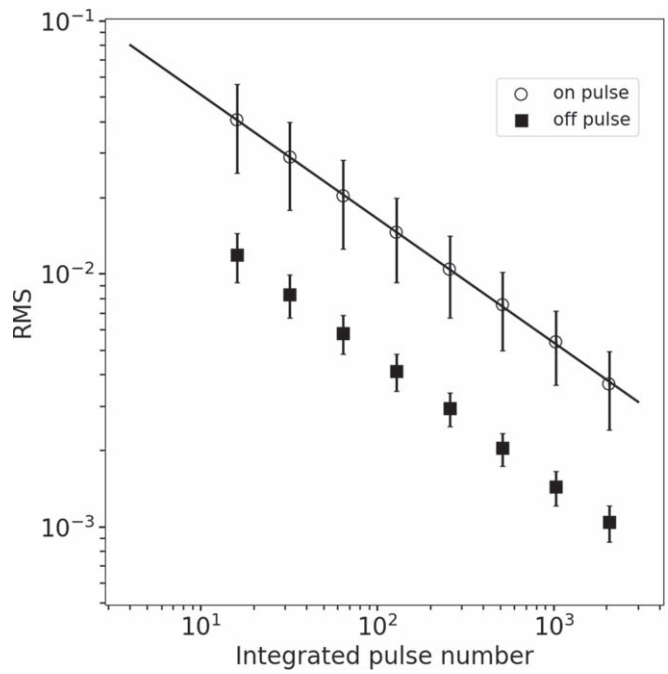

Figure 4. Root mean square (rms) values obtained from the difference between the profile formed for a given number of pulses and a template obtained using all available pulses. The open circles represent the rms values obtained in the on-pulse region. The solid black squares are obtained from the off-pulse region. The solid black line is the best-fitting model for the on-pulse data.

$N(E) = \frac{A}{E}\exp\left(-\frac{(\ln E - \mu)^2}{2\sigma^2}\right)$ where $\mu = -0.06 \pm 0.01$ and $\sigma = 0.51 \pm 0.01$ and A is normalization factor.

For each single pulse, we also measured the leading component pulse energy, E_l, using the area across the leading component region, as defined using the dotted horizontal line in Figure 1. Similarly, we measured trailing component pulse energy (defined by the dashed line in the figure). Figure 3 shows the correlation between the leading component pulse energy, E_l, and the trailing component pulse energy, E_t. The Pearson product-moment correlation coefficient of E_l and E_t is 0.38. The points do not fall on the $E_t = E_l$ line. The leading component is much wider in general, and, as a result, the leading component has more energy than that of the trailing component in most cases.

Liu et al. (2015) showed that the occurrence of subpulses (individual components of the single pulses) in the leading and trailing components of the PSR J1022+1001 profile is correlated. Their work was based on 14000 subpulses obtained over 35 hr, which is only 0.2% of the total number of pulses expected during that time period. They have therefore only selected the brightest pulses for their analysis. We note from our correlation that if the leading component energy is large, then the trailing component energy also tends to be large. This agrees with the results in Liu et al. (2015), but we note from our data that the components are only partially correlated.

3.2. Nulling and Giant Pulses

As shown in Figure 2, the energy distribution can be modeled used a single log-normal distribution. We would expect the energy distribution of nulling pulses is similar to that of the off-pulse region (the yellow histogram). However, we see no evidence of this with our data set. If we define nulling pulses to have on-pulse energy smaller than three times the standard deviation of the off-pulse energy, then this gives an upper limit of nulling fraction of 0.06%.

The pulse energy for normal pulses typically follows a log-normal or normal distribution. In comparison, the pulse energy for giant pulses generally follows a power-law distribution, e.g., the Crab pulsar (Staelin & Reifenstein 1968), PSR B1937+21 (Cognard et al. 1996) and PSR B0540−69 (Johnston & Romani 2003). In our data, the brightest pulse is only approximately four times the average. We therefore have no evidence that PSR J1022+1001 exhibits the giant pulse phenomenon.

3.3. Mode Changing

Mode changing behavior has previously only been seen in one other millisecond pulsar (PSR B1957+20). The switching cadence between the modes for that pulsar is ∼1000 pulses. This is similar to the mode-switching timescales found in normal, non-millisecond pulsars (but note these timescales are much shorter than the pulse variations identified for intermittent pulsars; e.g., Wang et al. 2020).

To determine whether PSR J1022+1001 shows mode changing, we averaged different numbers of individual pulses together to form pulse profiles. We then used the PSRCHIVE software package to compare the averaged pulse profiles with the template obtained by summing all the available data. We subtracted each profile from the phase aligned template and determined the root mean square (rms) values of the difference in the on-pulse region and in the off-pulse region. These rms values are plotted in Figure 4. We fitted a power law, $\mathrm{rms}(N) = AN^{\beta}$ (where N is the number of pulses that have been averaged), to the on-pulse rms values and obtained that $\beta = -0.49 \pm 0.01$. There is no indication from this figure that

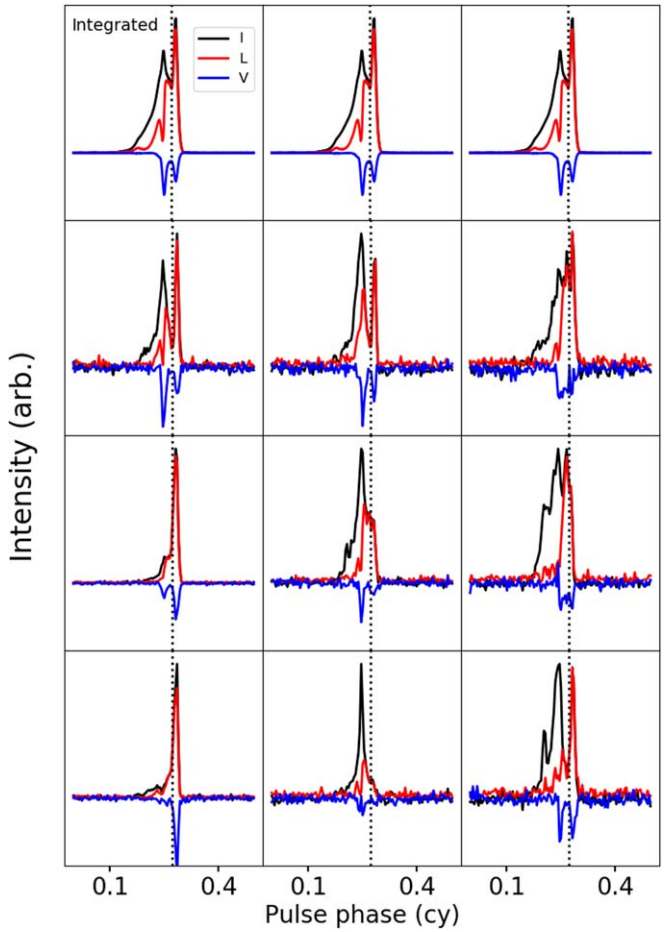

Figure 5. Single pulses from PSR J1022+1001. The first row shows the integrated pulse profile. The black, red, and blue lines represent Stokes *I*, the linear polarization, and Stokes *V*, respectively. The vertical dashed line separates the leading component and the trailing component. The left column shows three single pulses which have a brighter trailing component than the leading component. The middle column shows three single pulses which have a brighter leading component. The right column shows three single pulses which have multiple peaks.

PSR J1022+1001 undergoes profile changes on a timescale between ∼10 and ∼2000 pulses.

3.4. Single-pulse Polarization

The single pulses have a large variety of profile shapes. In Figure 5 we show polarization profiles for a few, representative, single pulses. The top row shows three copies of the integrated pulse profile. For the remaining nine panels, the left column contains three single pulses, which have a brighter trailing component than the leading component. The middle column shows three single pulses which have a brighter leading component. The right column shows three single pulses which have multiple peaks. When the leading component dominates, the trailing component varies from being almost as bright as the leading component, to being undetectable. The same is true when the trailing component dominates. We note that the trailing component is always highly linearly polarized, however, the leading component has a varying degree of linear polarization.

In order to determine the degree of correlation between the signal-to-noise ratio (S/N) for each pulse and its polarization fraction, we defined the degree of linear polarization as $(\Sigma_i\sqrt{Q_i^2+U_i^2})/(\Sigma_i I_i)$ and that of circular polarization as $(\Sigma_i|V_i|)/(\Sigma_i I_i)$, where Q, U, V are the Stokes parameters and the summation is over the phase bins in the on-pulse region. We determined the S/N as the integrated power in the pulse profile divided by the noise in the baseline. We then normalized these S/N values by dividing by the mean S/N value (giving S/N_n). Finally we divided the single pulses in S/N_n ranges in Table 1. Figure 6 shows the relation between S/N_n and the degrees of linear and circular polarization. The degrees of both linear and circular polarization increase with S/N_n. This agrees with similar dependencies observed in two other MSPs (Osłowski et al. 2014; Liu et al. 2016). We note an apparent increase in the linear polarization fraction at low S/N. This is also seen in the results presented by Osłowski et al. (2014) for PSR J0437−4715. Using Equation (22) in Day et al. (2020), we calculated uncertainties on the linear polarization fraction to be smaller than 0.3% for all points in the upper panel of Figure 6, thus this may represent some unexpected property of the low S/N pulses.

Table 1
S/N_n Ranges Used for Figure 6

Included Range	Number of Pulses	Fraction of Pulses
$0 < S/N_n < 0.50$	18533	0.2539
$0.50 < S/N_n < 0.66$	11428	0.1565
$0.66 < S/N_n < 0.87$	10923	0.1496
$0.87 < S/N_n < 1.16$	9346	0.1280
$1.16 < S/N_n < 1.53$	8705	0.1192
$1.53 < S/N_n < 2.03$	7359	0.1008
$2.03 < S/N_n < 2.68$	4562	0.0625
$2.68 < S/N_n < 3.54$	1759	0.0241
$3.54 < S/N_n < 4.69$	352	0.0048
$4.69 < S/N_n < 6.2$	33	0.0005

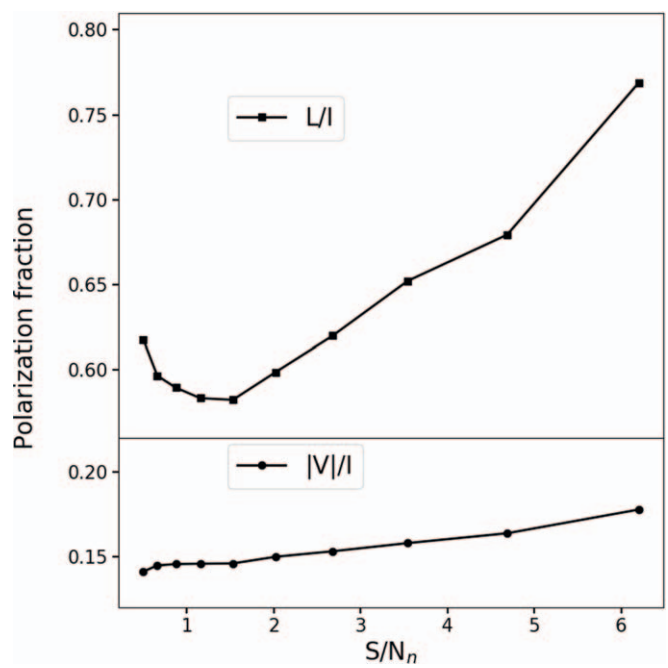

Figure 6. Polarization fractions of linear (top) and circular (bottom) component as a function of S/N_n.

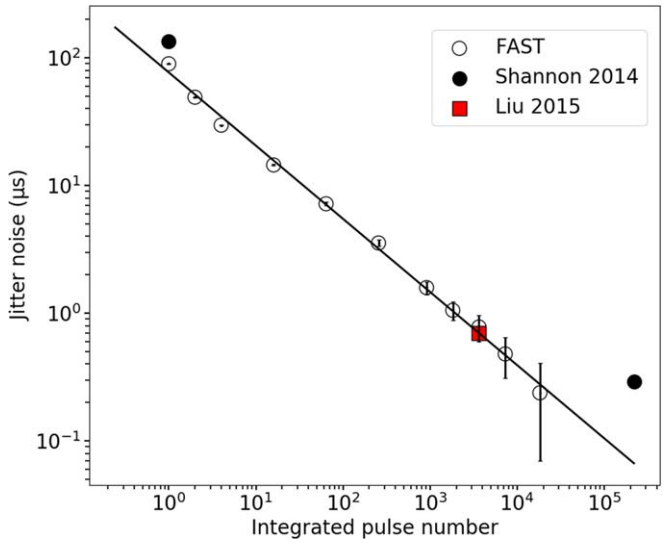

Figure 7. Estimates of jitter noise in PSR J1022+1001 from the FAST observation. Open circles are obtained with FAST using all single pulses. Solid black data points are the results in Shannon et al. (2014). The red square is the result from Liu et al. (2015). The solid black line is the best-fitting model for the jitter noise measured with FAST.

3.5. Pulse Jitter

PSR J1022+1001 is observed by pulsar timing array projects (e.g., Hobbs 2013; Kramer & Champion 2013; Manchester & IPTA 2013; Manchester et al. 2013), which have the primary goal of detecting ultra-low-frequency gravitational waves. The sensitivity of such an array depends upon the scatter in the timing residuals.

On short timescales the timing residuals are primarily dominated by radiometer noise (a reasonable representation is given by the ToA uncertainties) and pulse jitter (e.g., Osłowski et al. 2011; Liu et al. 2012, 2015; Shannon & Cordes 2012; Shannon et al. 2014; Lam et al. 2016). Following Shannon et al. (2014), we define the jitter noise level obtained after N pulses have been averaged together, $\sigma_{\rm J}(N)$, to be the quadrature difference between the rms of the timing residuals and the radiometer noise

$$\sigma_{\rm J}^2(N) = \sigma_{\rm obs}^2(N) - \sigma_{\rm radiometer}^2(N). \quad (1)$$

This assumes that all of the excess error in the arrival time measurements can be attributed to jitter noise. We used simulated data sets to obtain the radiometer noise. In these simulated data sets, we formed pulse profiles from the template obtained by summing all the available pulses and white noise such that the S/N of the simulated profile matched the S/N of the observed profile.

In Figure 7, we compare estimates of the jitter noise in PSR J1022+1001 from our FAST observation (open circles) with previous Parkes observations (Shannon et al. 2014), and from Westerbork Synthesis Radio Telescope and Effelsberg 100 m Radio Telescope observations (Liu et al. 2015). We fit a power law, $\sigma_{\rm J}(N) = AN^{\beta}$ to the jitter noise measured from our observations and obtain $\beta = -0.57 \pm 0.01$. The jitter noise level when scaled to one hour is 67 ± 9 ns. This value is significantly smaller than the value of 290 ± 15 ns reported in Shannon et al. (2014) (see black circles in Figure 7), but is consistent with Liu et al. (2015), which reported a jitter noise level of 700 ns based on continuous 1 minute integrations (red square in Figure 7). The discrepancy between our results and Shannon et al. (2014) may be caused by profile shape variations on hour-long timescales (which the Shannon et al. 2014 analysis probes). Such variations could be caused by the evolution of the pulse profile with frequency combined with the interstellar scintillation (Shao & You 2017).

3.6. Single-pulse Timing

In the left-hand panel of Figure 8 we show the timing residuals obtained using our standard template for this pulsar. This provides the indication of three differing states. However, the timing residuals change with different templates. In the right-hand panel we used a template obtained from the summation of the profiles that formed the most negative timing residuals in the left-hand panel. We note that the number of residuals in each state (and the residual level of the states) varies between the two panels.

Osłowski et al. (2014) and Liu et al. (2016) trialed methods to improve the timing residuals by selecting pulses based on their S/N (for PSRs J0437−4715 and J1713+0747, respectively). Following these studies, we divided our single pulses into the following S/N_n ranges: $S/N_n < 0.9$, $0.9 < S/N_n < 2.0$ and $S/N_n > 2.0$. We obtained a template by summing the single pulses from each S/N_n range, formed arrival times for the pulse and then timing residuals. The rms timing residual is shown in Figure 9 as a function of integration time. The rms residual values are higher for all of the S/N_n selections compared with simply using all of the available pulses. Although Osłowski et al. (2014) reported marginal reduction of rms residual by rejecting ∼1% of largest S/N single pulses, PSRs J0437−4715 in Osłowski et al. (2014) and J1713+0747 in Liu et al. (2016) agree with our results.

As PSR J1022+1001 is a multi-component pulsar and the two components have, on average, comparable average energies, we also divided the single pulses according to the energy of the leading component and the trailing component: the single pulses which have larger leading component energy constitute the first class and the remainder constitute the second class. We followed the process above to form new templates from these samples and produced timing residuals. The rms timing residuals as a function of integration time are shown in Figure 10. Again, we identify no improvement in the rms residuals through this selection. The single pulses which have larger leading component energy consist of 91% of all pulses, so the resulting rms timing residuals are close to those of all pulses.

4. Conclusions

We have reported on the detection and analysis of $\sim 10^5$ single pulses from PSR J1022+1001. This is only possible with the high sensitivity available using FAST. There is no indication that PSR J1022+1001 exhibits giant pulse, nulling, or traditional mode changing phenomena. The energy in the leading and trailing components of the integrated profile is shown to be correlated. The degree of both linear and circular polarization increases with the pulse flux density for individual pulses.

Jitter noise is a limiting source of noise at FAST and we have determined that the jitter noise for this pulsar, scaled to one hour, is 67 ns. Selecting single pulses in different S/N_n ranges, or according to relative energy of the leading and trailing

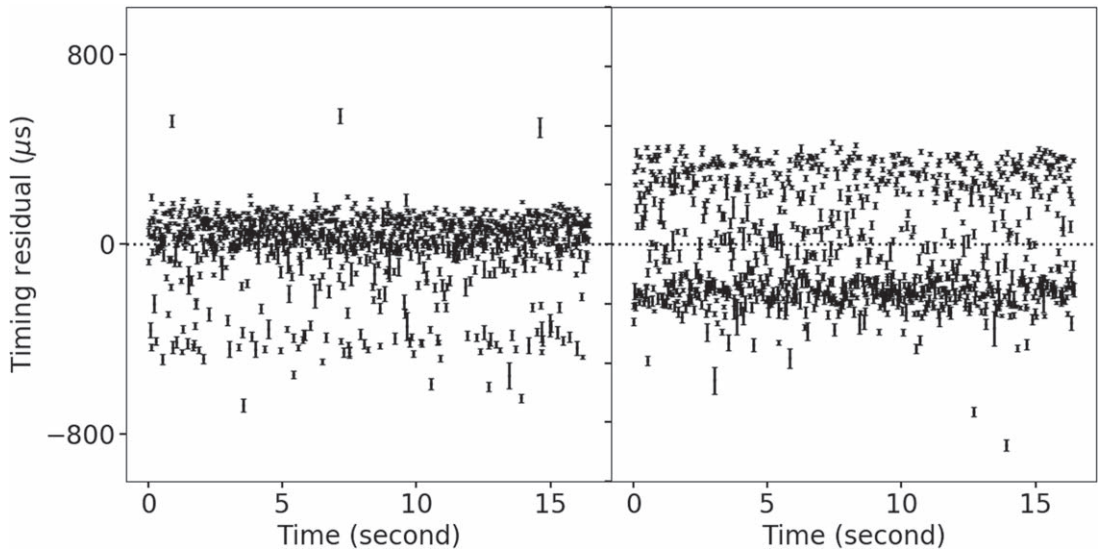

Figure 8. Left and right panels show the first 1000 timing residuals using different templates. We used the standard template in the left-hand panel. In the right-hand panel we used a template obtained from the summation of the profiles that formed the most negative timing residuals in the left-hand panel.

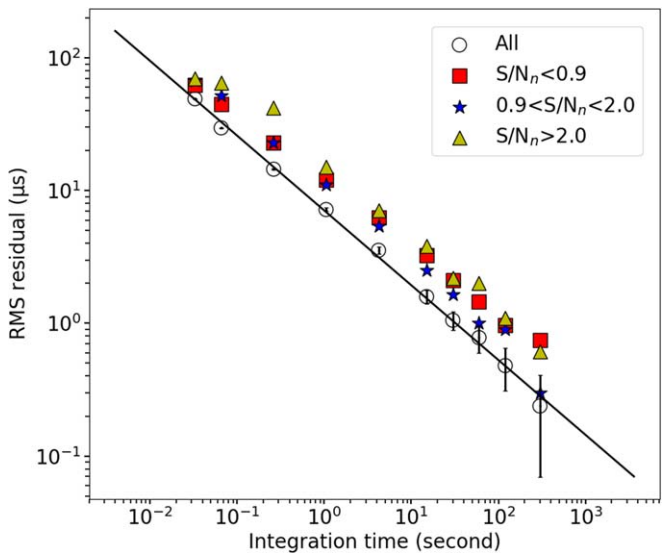

Figure 9. Rms timing residuals as a function of integration time obtained using all available pulses (open circles) and sub-sets determined from the specific S/N_n ranges (red, blue, and yellow symbols). The solid black line is the best-fitting model for the rms timing residual vs. integration time determined using all the available pulses.

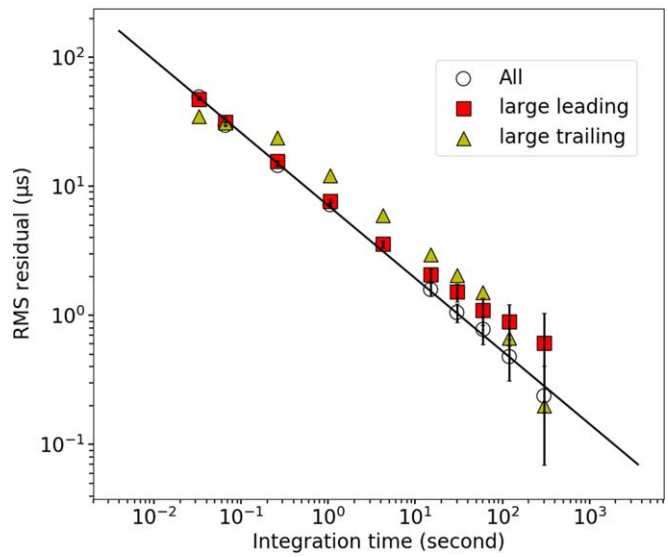

Figure 10. Rms timing residuals as a function of integration time obtained using all pulses (open circles) and sub-sets obtained from the pulses in which the leading component is larger than the trailing component (red square) and vice versa (yellow triangle). The solid black line is the best-fitting model to the open circles.

components, does not improve the timing precision achievable for PSR J1022+1001.

FAST provides us with the opportunity to study single pulses from millisecond pulsars in more detail than previously possible with the previous generation of radio telescopes. In the near future, FAST will be able to provide a catalog of single pulses from millisecond pulsars in the Northern Hemisphere and MeerKAT (and, in the near future, the Square Kilometer Array) will carry out similar work in the Southern Hemisphere. A detailed study of such single pulses may provide the opportunity to improve the sensitivity of pulsar timing array observations and for other key pulsar-related research, such as pulsar emission physics and testing theories of gravity.

We would like to thank R. M. Shannon, R. N. Manchester, M. Bailes, W. van Straten, and W. A. Coles for valuable discussions. We also thank the anonymous referee for providing constructive suggestions to improve the article. This work is supported by National Key R&D Program of China No. 2017YFA0402600, by the CAS International Partnership Program No.114- A11KYSB20160008, by the CAS Strategic Priority Research Program No. XDB23000000, and by NSFC grant Nos. 11725313 and 11690024. Y.F. is supported by China Scholarship Council. This work made use of the data from FAST (Five-hundred-meter Aperture Spherical radio Telescope). FAST is a Chinese national mega-science facility, operated by National Astronomical Observatories, Chinese Academy of Sciences.

Software: DSPSR (van Straten & Bailes 2011), PSRCHIVE (Hotan et al. 2004b), TEMPO2 (Hobbs et al. 2006).

ORCID iDs

Yi Feng https://orcid.org/0000-0002-0475-7479
D. Li https://orcid.org/0000-0003-3010-7661
S. Dai https://orcid.org/0000-0002-9618-2499
W. W. Zhu https://orcid.org/0000-0001-5105-4058
L. Qian https://orcid.org/0000-0003-0597-0957
L. Zhang https://orcid.org/0000-0001-8539-4237
S. Q. Wang https://orcid.org/0000-0003-4498-6070
Y.-K. Zhang https://orcid.org/0000-0002-8744-3546

References

Baars, J. W. M., Genzel, R., Pauliny-Toth, I. I. K., & Witzel, A. 1977, A&A, 500, 135
Backer, D. C. 1970, Natur, 228, 42
Bartel, N., Morris, D., Sieber, W., & Hankins, T. H. 1982, ApJ, 258, 776
Cognard, I., Shrauner, J. A., Taylor, J. H., & Thorsett, S. E. 1996, ApJL, 457, L81
Dai, S., Hobbs, G., Manchester, R. N., et al. 2015, MNRAS, 449, 3223
Day, C. K., Deller, A. T., Shannon, R. M., et al. 2020, MNRAS, 497, 3335
Drake, F. D., & Craft, H. D. 1968, Natur, 220, 231
Edwards, R. T., & Stappers, B. W. 2003, A&A, 407, 273
Hankins, T. H., Kern, J. S., Weatherall, J. C., & Eilek, J. A. 2003, Natur, 422, 141
Hobbs, G. 2013, CQGra, 30, 224007
Hobbs, G. B., Edwards, R. T., & Manchester, R. N. 2006, MNRAS, 369, 655
Hotan, A. W., Bailes, M., & Ord, S. M. 2004a, MNRAS, 355, 941
Hotan, A. W., van Straten, W., & Manchester, R. N. 2004b, PASA, 21, 302
Jenet, F. A., Anderson, S. B., & Prince, T. A. 2001, ApJ, 546, 394
Jiang, P., Yue, Y., Gan, H., et al. 2019, SCPMA, 62, 959502
Johnston, S., & Romani, R. W. 2003, ApJL, 590, L95
Keith, M. J., Coles, W., Shannon, R. M., et al. 2013, MNRAS, 429, 2161
Kerr, M., Reardon, D. J., Hobbs, G., et al. 2020, PASA, 37, e020
Kramer, M., & Champion, D. J. 2013, CQGra, 30, 224009
Kramer, M., Xilouris, K. M., Camilo, F., et al. 1999, ApJ, 520, 324
Lam, M. T., Cordes, J. M., Chatterjee, S., et al. 2016, ApJ, 819, 155
Li, D., & Pan, Z. 2016, RaSc, 51, 1060
Liu, K., Bassa, C. G., Janssen, G. H., et al. 2016, MNRAS, 463, 3239
Liu, K., Karuppusamy, R., Lee, K. J., et al. 2015, MNRAS, 449, 1158
Liu, K., Keane, E. F., Lee, K. J., et al. 2012, MNRAS, 420, 361
Lyne, A., Hobbs, G., Kramer, M., Stairs, I., & Stappers, B. 2010, Sci, 329, 408
Mahajan, N., van Kerkwijk, M. H., Main, R., & Pen, U.-L. 2018, ApJL, 867, L2
Manchester, R. N. & IPTA 2013, CQGra, 30, 224010
Manchester, R. N., Hobbs, G., Bailes, M., et al. 2013, PASA, 30, e017
Nan, R., Li, D., Jin, C., et al. 2011, IJMPD, 20, 989
Osłowski, S., van Straten, W., Bailes, M., Jameson, A., & Hobbs, G. 2014, MNRAS, 441, 3148
Osłowski, S., van Straten, W., Hobbs, G. B., Bailes, M., & Demorest, P. 2011, MNRAS, 418, 1258
Padmanabh, P. V., Barr, E. D., Champion, D. J., et al. 2020, MNRAS, 500, 1178
Shannon, R. M., & Cordes, J. M. 2012, ApJ, 761, 64
Shannon, R. M., Osłowski, S., Dai, S., et al. 2014, MNRAS, 443, 1463
Shao, M., & You, X.-p 2017, ChA&A, 41, 495
Staelin, D. H., & Reifenstein, E. C., III 1968, Sci, 162, 1481
Stairs, I. H., Lyne, A. G., Kramer, M., et al. 2019, MNRAS, 485, 3230
van Straten, W., & Bailes, M. 2011, PASA, 28, 1
Wang, N., Manchester, R. N., & Johnston, S. 2007, MNRAS, 377, 1383
Wang, S. Q., Wang, J. B., Hobbs, G., et al. 2020, ApJ, 897, 8
Weltevrede, P., Edwards, R. T., & Stappers, B. W. 2006, A&A, 445, 243